Monthly Notices
of the
ROYAL ASTRONOMICAL SOCIETY

MNRAS **460,** 3624–3636 (2016)
Advance Access publication 2016 May 29

doi:10.1093/mnras/stw1229

Accurate estimators of correlation functions in Fourier space

E. Sefusatti,[1,2]★ M. Crocce,[3] R. Scoccimarro[4] and H. M. P. Couchman[5]

[1]*INAF - Osservatorio Astronomico di Brera, via E. Bianchi 46, I-23807 Merate (LC), Italy*
[2]*INFN - Sezione di Padova, via Marzolo 8, I-35131 Padova, Italy*
[3]*Institut de Ciències de l'Espai, IEEC-CSIC, Campus UAB, Carrer de Can Magrans, s/n, E-08193 Bellaterra, Barcelona, Spain*
[4]*Center for Cosmology and Particle Physics, Department of Physics, New York University, New York, NY 10003, USA*
[5]*Department of Physics and Astronomy, McMaster University, Hamilton, ON L8S 4M1, Canada*

Accepted 2016 May 19. Received 2016 May 18; in original form 2016 January 13

ABSTRACT

Efficient estimators of Fourier-space statistics for large number of objects rely on fast Fourier transforms (FFTs), which are affected by aliasing from unresolved small-scale modes due to the finite FFT grid. Aliasing takes the form of a sum over images, each of them corresponding to the Fourier content displaced by increasing multiples of the sampling frequency of the grid. These spurious contributions limit the accuracy in the estimation of Fourier-space statistics, and are typically ameliorated by simultaneously increasing grid size and discarding high-frequency modes. This results in inefficient estimates for e.g. the power spectrum when desired systematic biases are well under per cent level. We show that using interlaced grids removes odd images, which include the dominant contribution to aliasing. In addition, we discuss the choice of interpolation kernel used to define density perturbations on the FFT grid and demonstrate that using higher order interpolation kernels than the standard Cloud-In-Cell algorithm results in significant reduction of the remaining images. We show that combining fourth-order interpolation with interlacing gives very accurate Fourier amplitudes and phases of density perturbations. This results in power spectrum and bispectrum estimates that have systematic biases below 0.01 per cent all the way to the Nyquist frequency of the grid, thus maximizing the use of unbiased Fourier coefficients for a given grid size and greatly reducing systematics for applications to large cosmological data sets.

Key words: methods: analytical – methods: data analysis – methods: numerical – methods: statistical – large-scale structure of Universe.

1 INTRODUCTION

A great effort is currently directed towards accurate measurements of the power spectrum of the galaxy distribution as a test of the cosmological model (see e.g. Laureijs et al. 2011; Levi et al. 2013). At the same time, theoretical predictions for the matter and galaxy power spectrum, which play a key role in the interpretation of observational data, are ultimately validated by measurements of such quantities in numerical simulations. Due to computational efficiency, Fourier-space statistics in simulations and galaxy surveys are usually computed using fast Fourier transforms (FFTs), which require building estimates of density or galaxy perturbations on a regular grid from the input data objects (*N*-body particles or galaxies). These Fourier coefficients are then used to calculate correlation functions in Fourier space such as the power spectrum or bispectrum.

However, introducing a discrete sampling as the FFT grid comes with limitations that can only be avoided under special circumstances. If the underlying spectrum of perturbations is bandwidth limited (vanishes above a cutoff frequency $k_{\rm max}$), then the sampling theorem guarantees that grid estimates are lossless as long as the sampling frequency of the grid ($k_s = 2\pi/H$, where H is the grid spacing) is at least twice the cutoff frequency, $k_s \geq 2k_{\rm max}$. This just says that the grid is fine enough so that every Fourier component in the signal is sampled at least twice per period, which intuitively makes sense (at least a peak and a trough is needed to resolve an oscillation).

Unfortunately, the conditions of the sampling theorem are not satisfied by cosmological perturbations, which have significant Fourier content at all frequencies. As a result of this, unresolved small-scale modes when sampled by the grid are mistakenly identified as modes supported by the grid, which results in spurious contamination of the FFT-determined Fourier coefficients that directly translates into a systematic error in e.g. the power spectrum and bispectrum. This contamination is known as *aliasing*: it takes the form of a sum over

★ E-mail: emiliano.sefusatti@brera.inaf.it.

© 2016 The Authors
Published by Oxford University Press on behalf of the Royal Astronomical Society

Downloaded from http://mnras.oxfordjournals.org/ at SISSA on October 12, 2016

images, each of them corresponding to the Fourier content displaced by increasing multiples of the sampling frequency of the grid k_s, as we shall discuss in detail below.

Aliasing can be removed entirely if the signal is first low-pass filtered so that only frequencies supported by the grid remain before sampling by the grid, effectively making the modified signal bandwidth limited. Although such process is not lossless (high frequencies are missing), the determination of the supported Fourier modes is free of systematics. Low-pass filtering, however, results in interpolating kernels that are very non-local in real space (a given object contributes to essentially all grid points), and thus the definition of perturbations on the grid becomes too computationally expensive to be useful despite the speedup of FFTs. The goal to minimize aliasing is therefore to design an interpolating kernel that is fairly local while at the same time acts as much as possible as a low-pass filter (i.e. it is fairly smooth). In this paper, we present an algorithm that achieves this for realistic spectra of cosmological perturbations. By working at the level of the Fourier modes, it simultaneously benefits all Fourier-space statistics.

The issue of aliasing in the measurements of the power spectrum has been addressed, in the specific context of cosmological studies, by Jing (2005), Cui et al. (2008), Yang et al. (2009), Colombi et al. (2009) and Jasche, Kitaura & Ensslin (2009). In particular, Jing (2005) derives the full expression, including the aliasing component, for the power spectrum measured from interpolation on a grid with a generic mass assignment scheme and proposes an iterative procedure to reduce the aliasing contribution based on the exact knowledge of the window function in Fourier space corresponding to such scheme. Cui et al. (2008) and Yang et al. (2009) do not attempt to correct for the error introduced by aliasing but search instead for an optimal assignment scheme able to reduce the effect. They identify for this purpose the scaling function of specific Daubechies wavelets and claim, as a result, a systematic error below the 2 per cent level for wavenumbers $k < 0.7 k_{\rm Nyq}$, $k_{\rm Nyq} \equiv k_s/2$ being the Nyquist frequency of the grid. A different approach is explored by Colombi et al. (2009) who consider a Fourier–Taylor expansion of the expression corresponding to a direct summation of the particle contribution to the density field in Fourier space. At the lowest order the procedure, implemented in the POWMES public code, corresponds to a Nearest Grid Point (NGP) assignment scheme but including higher order corrections it quickly converges to an unbiased estimator of the power spectrum, albeit at significant computational cost. Finally, Jasche et al. (2009) discuss a method based on 'supersampling' that inevitably increases memory requirements (typically by almost an order of magnitude).

In this paper, we revisit a technique based on interlacing two density grids that, while requiring only two times the number of density evaluations w.r.t. the standard case, can significantly reduce the aliasing contribution. The method is discussed in Hockney & Eastwood (1981), and has been implemented in the AP^{3}M N-body code for the mesh force calculation in Couchman (1991, see also Couchman 1999). Here, we show how it can be applied to the evaluation of the density field in Fourier space from point distributions. In particular, we quantify the relative effect of different mass assignment schemes on the aliasing contributions to the power spectrum estimation in two typical situations of cosmological interest: the non-linear matter distribution at low redshift from a small N-body simulation and the matter distribution obtained in the Zeldovich approximation (ZA) at high redshift. We proceed to illustrate the interlacing technique and we compare our results to Fourier coefficient evaluations by direct summation over objects (which are alias-free) and to the output of the POWMES public code.

The paper is organized as follows. Section 2 introduces and describes the problem of aliasing in mathematical terms, with specific attention to its interplay with the order of the mass assignment scheme adopted. Section 3 presents the interlacing technique and its effect on different power spectrum measurements. In Section 4, we quantify the contribution of aliasing with and without interlacing to higher order correlation functions such as the bispectrum. We present our conclusions in Section 5.

2 DENSITY ESTIMATION AND ALIASING

2.1 Correlation functions in Fourier space

We focus our attention on continuous fields defined over a finite, cubic volume $V = L^3$ which we will assume equivalent to the case of infinite volume but periodic with period L along each of the three spatial directions (the extension to the general case of a generic box of different periods while trivial, would require a significantly more cumbersome notation).

The matter density $\rho(\boldsymbol{x})$ can be described in terms of the dimensionless overdensity

$$\delta(\boldsymbol{x}) \equiv \frac{\rho(\boldsymbol{x})}{\bar{\rho}} - 1, \tag{1}$$

where $\bar{\rho}$ is the mean density in the volume V. Its Fourier space counterpart is given by

$$\delta(\boldsymbol{k}) \equiv \int_V \frac{d^3x}{(2\pi)^3}\, \mathrm{e}^{-i\boldsymbol{k}\cdot\boldsymbol{x}}\, \delta(\boldsymbol{x}), \tag{2}$$

while its inverse is defined in terms of the series

$$\delta(\boldsymbol{x}) \equiv k_{\rm f}^3 \sum_{\boldsymbol{k}} \mathrm{e}^{i\boldsymbol{k}\cdot\boldsymbol{x}}\, f(\boldsymbol{k}), \tag{3}$$

since $\boldsymbol{k}$ is discretized in multiples of the fundamental frequency $k_f = 2\pi/L$ in each spatial direction. Notice that we will always explicitly show the argument of each function in order to distinguish a real-space object from its Fourier transform.[1]

The power spectrum $P(k)$ is then defined as the two-point function of $\delta(\boldsymbol{k})$, that is

$$\langle \delta(\boldsymbol{k}_1)\, \delta(\boldsymbol{k}_2) \rangle \equiv \frac{\delta^K_{\boldsymbol{k}_{12}}}{k_{\rm f}^3}\, P(k_1), \tag{4}$$

with $\langle \dots \rangle$ representing the ensemble average, $\boldsymbol{k}_{i_1,\dots,i_n} \equiv \boldsymbol{k}_{i_1} + \dots + \boldsymbol{k}_{i_n}$ and $\delta^K_{\boldsymbol{k}}$ being a Kronecker delta defined to be equal to 1 for a vanishing argument $\boldsymbol{k} = 0$ and zero otherwise. Similarly, the bispectrum $B(k_1, k_2, k_3)$ is defined as

$$\langle \delta(\boldsymbol{k}_1)\, \delta(\boldsymbol{k}_2)\, \delta(\boldsymbol{k}_3) \rangle \equiv \frac{\delta^K_{\boldsymbol{k}_{123}}}{k_{\rm f}^3}\, B(k_1, k_2, k_3). \tag{5}$$

In this convention, the continuous limit is recovered for $V \to \infty$ or $k_{\rm f} \to 0$ with $\delta^K_{\boldsymbol{k}}/k_{\rm f}^3 \to \delta_{\rm D}(\boldsymbol{k})$, the latter being a Dirac delta function.

2.2 Direct summation

Theoretical predictions for the correlation functions of the matter density, or of the galaxy number density, often assume such

[1] In this convention for the Fourier transform, the Dirac delta in real space and the Kronecker delta in Fourier space are given, respectively, by the following representations:
$\delta_{\rm D}(\boldsymbol{x}) = \frac{1}{V}\sum_{\boldsymbol{k}} \mathrm{e}^{i\,\boldsymbol{k}\cdot\boldsymbol{x}}$ and $\delta^K_{\boldsymbol{k}} = \frac{1}{V}\int d^3x\, \mathrm{e}^{-i\,\boldsymbol{k}\cdot\boldsymbol{x}}$.

Downloaded from http://mnras.oxfordjournals.org/ at SISSA on October 12, 2016

quantities to be continuous random fields. However, in practical applications such as the analysis of N-body simulations or galaxy surveys they are given in terms of a finite number $N_{\rm P}$ of objects with positions $\{\boldsymbol{x}_i\}$ for $i = 1, \ldots, N_{\rm P}$. In this case, we can write the density as

$$\rho(\boldsymbol{x}) = \sum_{i=1}^{N_{\rm P}} m\, \delta_{\rm D}(\boldsymbol{x} - \boldsymbol{x}_i), \tag{6}$$

m being the particle mass which we assume here to be the same for all particles, for simplicity. It follows that

$$\delta(\boldsymbol{x}) = \frac{1}{\bar{n}} \sum_{i=1}^{N_{\rm P}} \delta_{\rm D}(\boldsymbol{x} - \boldsymbol{x}_i) - 1, \tag{7}$$

$\bar{n} \equiv N_{\rm P}/V$ being the particle density. The overdensity in Fourier space can be obtained by direct summation as the Fourier transform of the equation above, that is

$$\delta(\boldsymbol{k}) = \frac{1}{(2\pi)^3} \left[\frac{1}{\bar{n}} \sum_{i=1}^{N_{\rm P}} \mathrm{e}^{-i\,\boldsymbol{k}\cdot\boldsymbol{x}_i} - V\delta_{\boldsymbol{k}}^K \right]. \tag{8}$$

The Fourier-space two-point function defining the power spectrum is now given by

$$\langle\, \delta(\boldsymbol{k}_1)\, \delta(\boldsymbol{k}_2)\, \rangle = \frac{\delta^K_{k_{12}}}{k_{\rm f}^3} \left[P(k_1) + \frac{1}{(2\pi)^3\, \bar{n}} \right], \tag{9}$$

where the second term on the r.h.s. represents the shot-noise contribution due to the self-correlation of individual particles (see for instance, Peebles 1980; Jing 2005). The direct summation estimator for the power spectrum of a particle distribution is then

$$\hat{P}(k) \equiv k_{\rm f}^3\, |\delta(\boldsymbol{k})|^2 = k_{\rm f}^3 \left[|\delta(\boldsymbol{k})|^2 - \frac{1}{N_{\rm P}} \right], \tag{10}$$

and the true power spectrum is recovered as $P(k) = \langle \hat{P}(k) \rangle$.

Direct summation is clearly quite a demanding approach, particularly in the case of N-body simulations with a very large number of particles, since the evaluation of the Fourier-space density scales as $N_{\rm P} \times N_{\rm G}^3$, $N_{\rm G}^3$ being the number of wavenumbers $\boldsymbol{k}$ required. While impractical, it is however an exact alias-free determination of Fourier coefficients. Therefore, we shall use direct summation estimates below as a benchmark to which FFT methods are compared.

2.3 Mass assignment and aliasing

A more efficient method, taking advantage of the FFT algorithm, requires first the interpolation of the density field on a regular grid in position space. This fixes the largest wavenumber accessible to the Nyquist frequency, $k_{\rm Nyq} = \pi N_{\rm G}/L = \pi/H$, $N_{\rm G}$ being now the linear size of the grid and $H = L/N_{\rm G}$ therefore being the grid spacing. The price to pay is the emergence of aliasing in the Fourier transform of the density grid and therefore a systematic error that cannot be easily and completely removed from the measurements of the correlation functions in Fourier space. We will loosely revisit here the derivation by Jing (2005) of the theoretical expression for the power spectrum estimator based on grid interpolation and the FFT, since it will be useful to describe the interlacing method discussed in Section 3.

Let us assume $\boldsymbol{x}_j^G$ with $j = 1,...,N_{\rm G}^3$ to be a regular grid of points, for simplicity, linearly spaced by H in all directions. The interpolation of a continuous function $f(\boldsymbol{x})$ over the grid can be given by a simple integration over the cell of volume H^3 surrounding each point, so that

$$f(\boldsymbol{x}_j^G) = \frac{1}{H^3} \int_{\boldsymbol{x}_j^G} d^3x\, f(\boldsymbol{x}) \equiv \frac{1}{H^3} \int_{x_j^G - H/2}^{x_j^G + H/2} \mathrm{d}x \int_{y_j^G - H/2}^{y_j^G + H/2} \mathrm{d}y \int_{z_j^G - H/2}^{z_j^G + H/2} \mathrm{d}z\, f(\boldsymbol{x}). \tag{11}$$

In the case of the density defined by a particle distribution as in equation (6), each particle will provide a contribution only to the cell encompassing the particle position. As we will see, this simple procedure, known as the NGP assignment scheme, is not the optimal one. To consider more general schemes, it is convenient to assign a 'shape' to each particle defined by a function $S(\boldsymbol{x})$ which is symmetric, positive defined, separable as $S(\boldsymbol{x}) = S_{\rm 1D}(x)\, S_{\rm 1D}(y)\, S_{\rm 1D}(z)$, and normalized such that $\int d^3x\, S(\boldsymbol{x})/(2\pi)^3 = 1$. Separability makes computations efficient, since the resulting scheme will only need 1D distances in each direction, as opposed to e.g. spherically symmetric shapes which require radial distances to be computed. Similarly, correcting for the interpolation window in Fourier space is straightforward when separability is assumed.

The interpolation over the grid corresponds then to the evaluation of the (continuous) function

$$\widetilde{\delta}(\boldsymbol{x}) \equiv \int \frac{d^3x'}{(2\pi)^3}\, W(\boldsymbol{x} - \boldsymbol{x}')\, \delta(\boldsymbol{x}') \tag{12}$$

at the grid points $\boldsymbol{x}_j^G$, leading to

$$\widetilde{\delta}(\boldsymbol{x}_j^G) = \frac{1}{(2\pi)^3 \bar{n}} \sum_{i=1}^{N_P} W\left(\boldsymbol{x}_j^G - \boldsymbol{x}_i\right) - 1, \tag{13}$$

where the weight function $W(\boldsymbol{x})$ is simply the integral over the cell volume of the shape function $S(\boldsymbol{x})$ given by

$$W(\boldsymbol{x}_j^G - \boldsymbol{x}_i) = \frac{1}{H^3} \int_{\boldsymbol{x}_j^G} d^3x\, S(\boldsymbol{x} - \boldsymbol{x}_i). \tag{14}$$

In addition to the NGP, assignment schemes commonly adopted are the Cloud-In-Cell (CIC) and Triangular Shape Cloud (TSC) scheme, representing the lowest order piecewise polynomial function (also known as B-splines). They correspond, respectively, to first, second and third order referring to the number p of grid points, per dimension, to which each particle is assigned. The relative piecewise polynomial functions $W^{(p)}$ are of order less or equal to $(p - 1)$, and correspond simply to convolving a top-hat function with itself $(p - 1)$ times. The weights are then given explicitly by $W(\boldsymbol{x}) = W^{(p)}(x/H)\, W^{(p)}(y/H)\, W^{(p)}(z/H)$, where for each different scheme we have the one-dimensional functions:

(i) NGP

$$W^{(1)}(s) = \begin{cases} 1 \text{ for } |s| < \frac{1}{2} \\ 0 \text{ otherwise} \end{cases} \tag{15}$$

(ii) CIC

$$W^{(2)}(s) = \begin{cases} 1 - |s| \text{ for } |s| < \frac{1}{2} \\ 0 \qquad\quad \text{otherwise} \end{cases} \tag{16}$$

(iii) TSC

$$W^{(3)}(s) = \begin{cases} \frac{3}{4} - s^2 & \text{for } |s| < \frac{1}{2} \\ \frac{1}{2}\left(\frac{3}{2} - |s|\right)^2 & \text{for } \frac{1}{2} \le |s| < \frac{3}{2} \\ 0 & \text{otherwise,} \end{cases} \tag{17}$$

Downloaded from http://mnras.oxfordjournals.org/ at SISSA on October 12, 2016

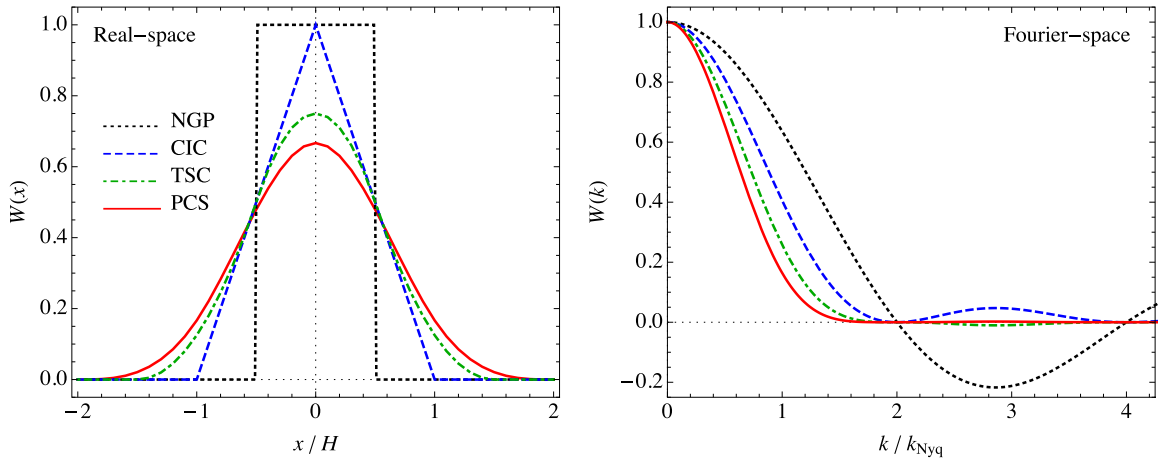

Figure 1. Left-hand panel: one-dimensional, real-space window functions $W^{(p)}(x)$ of the four mass assignment schemes described in the text. Different curves show NGP (dotted, black), CIC (dashed, blue), TSC (dot–dashed, green) and PCS interpolation (continuous, red). Right-hand panel: the same window functions in Fourier space, $W^{(p)}(k)$.

where $s = (x_j^G - x)/H$. Clearly, schemes of order higher than TSC can be considered (as it is often the case in plasma physics applications, see e.g. Haugbølle, Frederiksen & Nordlund 2013). Here, we will consider only the next, fourth-order interpolation scheme, which we will refer to as Piecewise Cubic Spline (PCS; see e.g. Chaniotis & Poulikakos 2004, for generic, higher order B-spline interpolation). The corresponding weights are given by

(i) PCS

$$W^{(4)}(s) = \begin{cases} \frac{1}{6}\left(4 - 6\,s^2 + 3\,|s|^3\right) & \text{for } 0 \le |s| < 1 \\ \frac{1}{6}\left(2 - |s|\right)^3 & \text{for } 1 \le |s| < 2 \\ 0 & \text{otherwise.} \end{cases} \tag{18}$$

In the left-hand panel of Fig. 1, we show the one-dimensional window functions in real space $W^{(p)}(x)$ where it is evident how the support of the weight function grows with the interpolation order.

The sampling in real space given by equation (13) can be mathematically described in terms of the sampling function Ш $(\boldsymbol{x})$ (see e.g. Hockney & Eastwood 1981). This is defined as

$$\text{Ш}(\boldsymbol{x}) = \sum_{\boldsymbol{n}} \delta_{\rm D}(\boldsymbol{x} - \boldsymbol{n}), \tag{19}$$

with $\boldsymbol{n}$ an integer vector. It is easy to see that the Fourier transform of $\widetilde{\delta}(\boldsymbol{x}_j^G)$ is equal to the Fourier transform of the continuous field given by the product $\text{Ш}(\boldsymbol{x}/H)\,\widetilde{\delta}(\boldsymbol{x})$ which is different from zero only for $\boldsymbol{x} = \boldsymbol{x}_j^G$ and equals $\widetilde{\delta}(\boldsymbol{x}_j^G)$ at those points when integrated over. Applying the convolution theorem, we obtain

$$\widetilde{\delta}^{\rm G}(\boldsymbol{k}) = k_{\rm f}^3 \sum_{\boldsymbol{k}'} \text{Ш}(\boldsymbol{k}')\,\widetilde{\delta}(\boldsymbol{k} - \boldsymbol{k}'), \tag{20}$$

where $\widetilde{\delta}(\boldsymbol{k})$ is the Fourier transform of the convolved, continuous density field defined in equation (12), while $\widetilde{\delta}^G(\boldsymbol{k})$, in addition, accounts for the discreteness of the grid assignment.

We notice now that the Fourier transform of the sampling function is a sampling function in k-space. Since we are dealing with periodic functions in position space, the Delta functions are replaced by Kronecker deltas as

$$\text{Ш}(\boldsymbol{k}) = \frac{1}{k_{\rm f}^3} \sum_{n} \delta^K_{\boldsymbol{k} - \boldsymbol{n}\,k_s}, \tag{21}$$

where the sampling frequency of the grid k_s is given by

$$k_s \equiv \frac{2\pi}{H} \tag{22}$$

so that we obtain

$$\widetilde{\delta}^{\rm G}(\boldsymbol{k}) = \sum_{\boldsymbol{n}} \widetilde{\delta}\,(\boldsymbol{k} - \boldsymbol{n}\,k_s)\,, \tag{23}$$

where clearly $\widetilde{\delta}^{\rm G}$ is k_s-periodic and we are thus interested in frequencies $|\boldsymbol{k}| \le k_s/2 = k_{\rm Nyq} = \pi/H = \pi\,N_{\rm G}/L$, with $k_{\rm Nyq}$ the Nyquist frequency of the grid. In this expression, all terms with $\boldsymbol{n} \neq 0$ in the sum represent the aliasing contribution to the estimate $\widetilde{\delta}^{\rm G}(\boldsymbol{k})$ of the density $\widetilde{\delta}(\boldsymbol{k})$, which, we should keep in mind, includes the effect of the interpolation function $W(\boldsymbol{x})$. Such effects can be removed from the leading contribution in the sum above, simply dividing by the FT of the window function itself, $W(\boldsymbol{k})$. The *corrected*, grid-based density contrast would then be given by

$$\delta^{\rm G}(\boldsymbol{k}) \equiv \frac{\widetilde{\delta}^{\rm G}(\boldsymbol{k})}{W(\boldsymbol{k})} = \frac{1}{W(\boldsymbol{k})} \sum_{\boldsymbol{n}} \widetilde{\delta}\,(\boldsymbol{k} - \boldsymbol{n}\,k_s)\,, \tag{24}$$

and introducing the 'corrected' window function

$$w_{\boldsymbol{n}}(\boldsymbol{k}) \equiv \frac{W(\boldsymbol{k} - \boldsymbol{n}\,k_s)}{W(\boldsymbol{k})}, \tag{25}$$

defined in such a way that $w_0(\boldsymbol{k}) = 1$, we obtain

$$\delta^{\rm G}(\boldsymbol{k}) = \delta\,(\boldsymbol{k}) + \sum_{\boldsymbol{n}\neq\boldsymbol{0}} w_{\boldsymbol{n}}(\boldsymbol{k})\,\delta\,(\boldsymbol{k} - \boldsymbol{n}\,k_s)\,, \tag{26}$$

where indeed the $\boldsymbol{n} = 0$ term provides the desired estimation of the density $\delta(\boldsymbol{k})$, while all other terms correspond to spurious, aliasing contributions. They correspond to 'images' of the Fourier content $\delta(\boldsymbol{k})$ centred at increased multiples of the sampling frequency of the grid k_s. For the frequencies of interest, $|\boldsymbol{k}| \le k_s/2 = k_{\rm Nyq}$, the images correspond to small-scale modes not supported by the grid that masquerade as modes of the frequency range we are interested in. These unwanted contributions have an amplitude that depends not only on the small-scale power but also on the weight given by the corrected window function $w_{\boldsymbol{n}}$.

Our main goal here is therefore to minimize $w_{\boldsymbol{n}}$ subject to the constraints of computational speed. Ideally, as pointed out in the

Downloaded from http://mnras.oxfordjournals.org/ at SISSA on October 12, 2016

introduction, to remove aliasing one would choose an interpolation function $W(k)$ which is a low-pass filter for modes of frequency less than k_s, which would automatically make the $w_{\boldsymbol{n}}$ vanish. The drawback of this choice is that the real-space kernel is then very non-local and that makes inefficient the interpolation to the grid, since each object would contribute to a large number of grid points. This, in effect, would constitute the bottleneck of the computational cost, and would negate the whole point of using FFTs as opposed to direct summation. The objective is then to find interpolation kernels that are sufficiently local in both real and Fourier space.

In order to highlight these aspects, on the right-hand panel of Fig. 1 we show the (one-dimensional) window functions in Fourier space $W(k)$. For the B-spline windows considered above these are simply given by

$$W^{(p)}(k) = \left[\frac{\sin(kH/2)}{(kH/2)}\right]^p = \left[\frac{\sin(\pi\, k/k_s)}{(\pi\, k/k_s)}\right]^p, \tag{27}$$

$p = 1$–4 being the interpolation order corresponding to NGP, CIC, TSC and PCS. Again, equation (27) makes clear that the different interpolation schemes correspond to convolutions of $(p-1)$ top-hat functions in 1D. For the 3D case, due to the separability assumption, one simply multiplies three such objects for each dimension, which is quite efficient. It is clear from Fig. 1 that the PCS kernel satisfies the opposite requirements of compactness in real and Fourier space rather well, although there is of course a tradeoff. The Fourier-space compactness means that the amplitude of the unwanted images $w_{\boldsymbol{n}}$ will be highly suppressed, this comes at the expense of a slightly more expensive interpolation to the grid as the real-space kernel is correspondingly broader. We will examine the impact of these choices for the power spectrum and bispectrum below.

As mentioned above, any aliasing correction to the density field will inevitably affect the estimation of any correlation function. In the first place, the two-point function of the interpolated, corrected density field $\delta^{\rm G}(\boldsymbol{k})$, will be given by

$$\langle\, \delta^{\rm G}(\boldsymbol{k}_1)\, \delta^{\rm G}(\boldsymbol{k}_2)\,\rangle = \sum_{\boldsymbol{n}_1,\,\boldsymbol{n}_2} w_{\boldsymbol{n}_1}(\boldsymbol{k}_1)\, w_{\boldsymbol{n}_2}(\boldsymbol{k}_2) \times \langle\, \delta(\boldsymbol{q}_1)\, \delta(\boldsymbol{q}_2)\,\rangle, \tag{28}$$

where $\boldsymbol{q}_i = \boldsymbol{k}_i - \boldsymbol{n}_i\, k_s$ and where the expectation value on the r.h.s. coincides with the one of equation (9).

The relation between the power spectrum estimated from the grid-based density $\delta^{\rm G}$ and the desired power spectrum $P(k)$ of the original distribution is then given by

$$P^{\rm G}(k) \equiv k_{\rm f}^3\, \langle\, |\delta^{\rm G}(\boldsymbol{k})|^2\,\rangle = \sum_{\boldsymbol{n}} |w_{\boldsymbol{n}}(\boldsymbol{k})|^2\; P_{\rm tot}\,(|\boldsymbol{k} - \boldsymbol{n}\, k_s|)\,, \tag{29}$$

where $P_{\rm tot}(k) \equiv P(k) + 1/[(2\pi)^3\, \bar{n}]$, an expression first derived by Jing (2005), here corrected for the window effects at leading order in the aliasing expansion.

In the case of the bispectrum $B^{\rm G}(k_1, k_2, k_3)$, we obtain the similar expression,

$$\begin{aligned} B^{\rm G}(k_1, k_2, k_3) &= \sum_{\boldsymbol{n}_1,\,\boldsymbol{n}_2,\,\boldsymbol{n}_3} w_{\boldsymbol{n}_1}(\boldsymbol{k}_1)\, w_{\boldsymbol{n}_2}(\boldsymbol{k}_2)\, w_{\boldsymbol{n}_3}(\boldsymbol{k}_3) \\ &\quad \times \delta^K_{q_{123}}\, B_{\rm tot}(q_1, q_2, q_3) \\ &= \sum_{\boldsymbol{n}_1,\,\boldsymbol{n}_2} w_{\boldsymbol{n}_1}(\boldsymbol{k}_1)\, w_{\boldsymbol{n}_2}(\boldsymbol{k}_2)\, w_{-\boldsymbol{n}_{12}}(-\boldsymbol{k}_{12}) \\ &\quad \times B_{\rm tot}(\boldsymbol{k}_1 - \boldsymbol{n}_1\, k_s, \boldsymbol{k}_2 - \boldsymbol{n}_2\, k_s), \end{aligned} \tag{30}$$

where

$$B_{\rm tot} \equiv B(k_1, k_2, k_3) + \frac{1}{(2\pi)^3\, \bar{n}}\, [P(k_1) + P(k_2) + P(k_3)] + \frac{1}{(2\pi)^6\, \bar{n}^2}, \tag{31}$$

and where, again, only the leading term for $\boldsymbol{n}_1 = \boldsymbol{n}_2 = \boldsymbol{n}_3 = 0$ corresponds to the desired estimated bispectrum (plus shot-noise), while all the others provide unwanted aliasing contributions.

Jing (2005) proposes a procedure to correct for the aliasing contribution to the power spectrum by means of a function that requires, in principle, a priori knowledge of the target power spectrum itself. Since, however, such knowledge is relevant only for values close to the Nyquist frequency, a power-law approximation of the power spectrum, determined by an iterative scheme, is employed instead. While this could provide a reasonable and effective solution to the problem of aliasing in power spectrum estimation, the procedure cannot be easily extended to the bispectrum, where one would need a model to describe the scale and triangle-shape dependence of high-k modes to effectively handle such corrections.

We will explore, in the rest of the paper, a more flexible alternative.

3 ALIASING REDUCTION BY INTERLACING

3.1 Interlacing

A method to partially correct for aliasing based on the interlacing of two grid is discussed in Hockney & Eastwood (1981), and its implementation in the AP^{3}M N-body code by Couchman (1991) for the mesh force calculation is mentioned in Couchman (1999).

We have seen that, for a generic mass assignment scheme, the interpolated density field, denoted below as $\widetilde{\delta}^{\rm G}_1(\boldsymbol{k})$, can be written as in equation (23), which we reproduce here for convenience

$$\begin{aligned} \widetilde{\delta}^{\rm G}_1(\boldsymbol{k}) &= \int_V \frac{d^3x}{(2\pi)^3}\, {\rm e}^{-i\,\boldsymbol{k}\cdot\boldsymbol{x}}\, {\rm Ш}\left(\frac{\boldsymbol{x}}{H}\right)\, \widetilde{\delta}(\boldsymbol{x}) \\ &= \sum_{\boldsymbol{n}} \widetilde{\delta}\,(\boldsymbol{k} - \boldsymbol{n}\, k_s)\,. \end{aligned} \tag{32}$$

An additional, real-space interpolation on a grid shifted by the distance $H/2$ in all spatial directions, with respect to the one above can be written as

$$\widetilde{\delta}^{\rm G}_2(\boldsymbol{k}) = \int_V \frac{d^3x}{(2\pi)^3}\, {\rm e}^{-i\,\boldsymbol{k}\cdot\boldsymbol{x}}\, {\rm Ш}\left(\frac{\boldsymbol{x}}{H} + \frac{1}{2}\right)\, \widetilde{\delta}(\boldsymbol{x})\,. \tag{33}$$

Again, since this represents the FT of a product, it can be written as a convolution of Fourier series, where, this time, the transform of the sampling function, equation (21), is obtained taking advantage of the shift theorem so that

$$\begin{aligned} \widetilde{\delta}^{\rm G}_2(\boldsymbol{k}) &= k_{\rm f}^3 \sum_{\boldsymbol{k}'} {\rm e}^{-i\,(k'_x + k'_y + k'_z)\, H/2}\, {\rm Ш}(\boldsymbol{k}')\, \widetilde{\delta}(\boldsymbol{k} - \boldsymbol{k}') \\ &= \sum_{\boldsymbol{n}} {\rm e}^{-\pi\, i\, (n_x + n_y + n_z)}\, \widetilde{\delta}\,(\boldsymbol{k} - \boldsymbol{n}\, k_s) \\ &= \sum_{\boldsymbol{n}} (-1)^{n_x + n_y + n_z}\, \widetilde{\delta}\,(\boldsymbol{k} - \boldsymbol{n}\, k_s)\,. \end{aligned} \tag{34}$$

Considering now the linear combination of the two, one obtains

$$\begin{aligned} \widetilde{\delta}^{\rm G}(\boldsymbol{k}) &= \frac{1}{2}\left[\widetilde{\delta}^{\rm G}_1(\boldsymbol{k}) + \widetilde{\delta}^{\rm G}_2(\boldsymbol{k})\right] \\ &= \sum_{\boldsymbol{n}} \theta_{\boldsymbol{n}}\, \widetilde{\delta}\,(\boldsymbol{k} - \boldsymbol{n}\, k_s)\,, \end{aligned} \tag{35}$$

Downloaded from http://mnras.oxfordjournals.org/ at SISSA on October 12, 2016

where we defined

$$\theta_{\boldsymbol{n}} \equiv \frac{1}{2}\left[1+(-1)^{n_x+n_y+n_z}\right] = \begin{cases} 1 & \text{for } n_x+n_y+n_z \text{ even} \\ 0 & \text{for } n_x+n_y+n_z \text{ odd.} \end{cases} \quad (36)$$

In the expression of equation (35) for the interlaced density all aliasing contributions (images) corresponding to odd values of the sum $n_x + n_y + n_z$, including, in particular, the largest ones for $|\boldsymbol{n}| = 1$ are removed. Clearly, the density field thus obtained should still be corrected for the effects of the window function as in equation (24), so that $\delta^G(\boldsymbol{k}) = \widetilde{\delta}^G(\boldsymbol{k})/W(\boldsymbol{k})$. In principle, the scheme could be extended to the combination of more than two interpolated density grids to remove the leading aliasing contributions at the next order.

The power spectrum of the interlaced density field, corrected for the window function, can now be written as

$$P^{\rm G}(k) = \sum_{\boldsymbol{n}} \theta_{\boldsymbol{n}} \, |w_{\boldsymbol{n}}(\boldsymbol{k})|^2 \, P_{\rm tot}\left(|\boldsymbol{k}-\boldsymbol{n}\,k_s|\right), \quad (37)$$

while the expression for the power spectrum of the (not interlaced) field of equation (29) is then recovered substituting $\theta_{\boldsymbol{n}}$ with 1 in the equation above.

We can write the residual aliasing contribution as

$$\Delta P^{\rm G}(k) \equiv P^{\rm G}(k) - P_{\rm tot}(k) = \sum_{\boldsymbol{n}\neq 0} \theta_{\boldsymbol{n}} \, |w_{\boldsymbol{n}}(\boldsymbol{k})|^2 \, P_{\rm tot}(\boldsymbol{k}-\boldsymbol{n}\,k_s). \quad (38)$$

Assuming that, for all $k > k_{\rm Nyq}$, the power spectrum has an upper bound $P_{\rm max} \geq P(k)$, the residual is, in turn, bounded as

$$\Delta P^{\rm G}(k) \leq \left[P_{\rm max} + \frac{1}{(2\pi)^3\,\bar{n}}\right] F_{\rm res}(\boldsymbol{k}), \quad (39)$$

where we introduce the residual factor $F_{\rm res}(\boldsymbol{k})$ on the r.h.s., defined as

$$F_{\rm res}(\boldsymbol{k}) \equiv \sum_{\boldsymbol{n}\neq 0} \theta_{\boldsymbol{n}} \, |w_{2\boldsymbol{n}}(\boldsymbol{k})|^2. \quad (40)$$

For mass assignment schemes corresponding to B-splines as those considered before, it is possible to evaluate this residual factor explicitly. For the interpolation order p, we have

$$F_{\rm res}(\boldsymbol{x}) = \sum_{\boldsymbol{n}\neq 0} \theta_{\boldsymbol{n}} \prod_{i=1}^{3} \left(\frac{x_i}{x_i - n_i}\right)^{2p}, \quad (41)$$

where $\boldsymbol{x} \equiv \boldsymbol{k}/k_s$ and the product runs over the three spatial dimensions. With no interlacing we obtain, more simply

$$F_{\rm res}(\boldsymbol{x}) = \sum_{\boldsymbol{n}\neq 0} \prod_{i=1}^{3} \left(\frac{x_i}{x_i - n_i}\right)^{2p}. \quad (42)$$

We note that in these expressions, a relatively small number of terms are enough to recover a reasonable accuracy.

Fig. 2 shows, for simplicity in one spatial dimension, the function $F_{\rm res}(k)$ for the four interpolation schemes assumed in the previous section, evaluated with and without interlacing. The figure nicely illustrates both the effects due to the choice of the interpolation scheme and due to the interlacing procedure. In the interlacing case, the 1D residual function explicitly corresponds to

$$F^{\rm int}_{\rm res,1D}(x) = \sum_{n\neq 0} \left(\frac{x}{x-2n}\right)^{2p} = \left(\frac{x}{2}\right)^{2p} \left[\zeta\left(2p,\, x/2\right) + \zeta\left(2p,\, -x/2\right)\right] - 2, \quad (43)$$

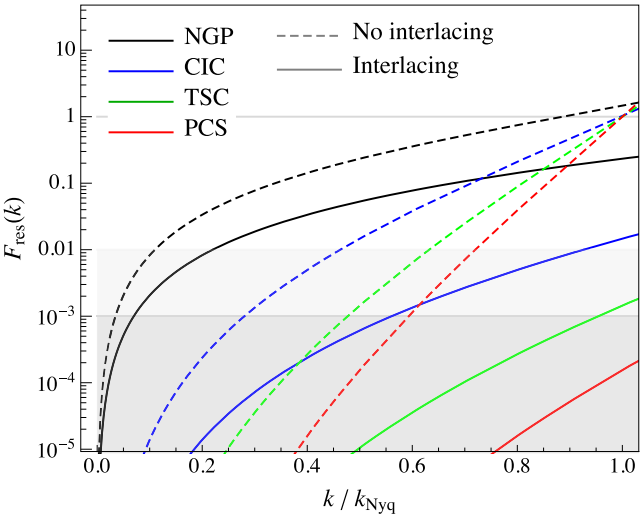

Figure 2. Residual factor $F_{\rm res,\,1D}(k)$, in one spatial dimension, as a function of the ratio of the wavenumber k to the Nyquist frequency, evaluated for the four interpolation schemes considered. Continuous and dashed curves assume, respectively, results with and without interlacing, equation (43) and equation (45), respectively.

where we introduced the Hurwitz zeta function

$$\zeta(p,x) = \sum_{n=0}^{\infty} \frac{1}{(n+x)^p}. \quad (44)$$

Without interlacing we have instead

$$F^{\rm no-int}_{\rm res,1D}(x) = \sum_{n\neq 0} \left(\frac{x}{x-n}\right)^{2p} = x^{2p}\left[\zeta\left(2\,p,\, x\right) + \zeta\left(2\,p,\, -x\right)\right] - 2. \quad (45)$$

We therefore obtain, in one dimension, the simple relation

$$F^{\rm int}_{\rm res,1D}(x) = F^{\rm no-int}_{\rm res,1D}(x/2). \quad (46)$$

Fig. 2 indicates in particular, as we will show with numerical tests in the next sections, that without interlacing, the aliasing contribution reaches relevant values approaching the Nyquist frequency $k_{\rm Nyq}$, regardless of the mass assignment scheme chosen. With interlacing, according to equation (46), this will happen at k equal twice $k_{\rm Nyq}$, i.e. well outside the interval of interest.

In a similar way, we can write the bispectrum of the interlaced field as

$$B^G(\boldsymbol{k}_1,\boldsymbol{k}_2) = \sum_{\boldsymbol{n}_1,\boldsymbol{n}_2} \theta_{\boldsymbol{n}_1}\,\theta_{\boldsymbol{n}_2}\,\theta_{-\boldsymbol{n}_{12}} \times w_{\boldsymbol{n}_1}(\boldsymbol{k}_1)\,w_{\boldsymbol{n}_2}(\boldsymbol{k}_2)\,w_{-\boldsymbol{n}_{12}}(-\boldsymbol{k}_{12}) \times B_{tot}(\boldsymbol{k}_1-\boldsymbol{n}_1\,k_s, \boldsymbol{k}_2-\boldsymbol{n}_2\,k_s), \quad (47)$$

where the residual aliasing contributions correspond to all terms in the sums with $\boldsymbol{n}_1 \neq 0$ and $\boldsymbol{n}_1 \neq 0$. In this case, we could not find a simple expression taking advantage of the explicit form of the B-spline window functions. We will present a numerical estimate of the aliasing contribution to the bispectrum in Section 4.

As a matter of fact, it is important to stress that the aliasing reduction is obtained, by interlacing, at the level of the density field, not after the power spectrum evaluation. As we will see, this fact ensures that the method benefits extend to all higher order correlations that can be estimated from the FT of field itself. Also,

Downloaded from http://mnras.oxfordjournals.org/ at SISSA on October 12, 2016

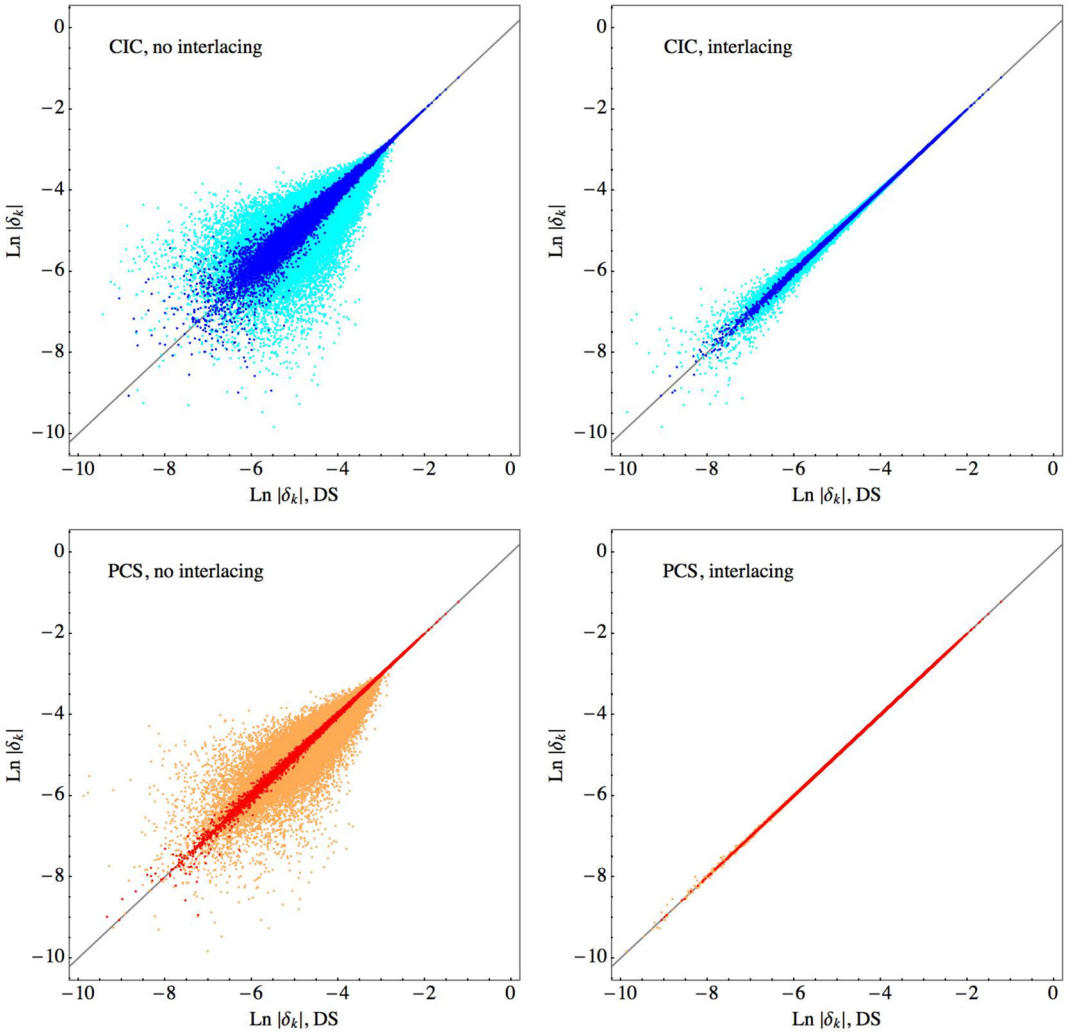

Figure 3. Scatter plots comparing the (log) amplitude of the Fourier-space density, $\ln|\delta(\boldsymbol{k})|$ obtained by interpolation on a grid and the same quantity obtained by direct summation. Top row assumes the CIC mass assignment scheme, while bottom row the PCS mass assignment scheme. Left-hand column assumes no correction by interlacing, while the right-hand column does. In all panels, light shaded (cyan and orange) points correspond to all modes in the grid of linear size $N_{\rm G} = 100$ while dark shaded (blue and red) points are restricted to modes of $|\boldsymbol{k}| \leq 0.7\, k_{\rm Nyq}$.

since interlacing only removes the odd images, it is important to supplement this technique with a reasonable choice of interpolation kernel as discussed in the previous section to suppress the amplitude of the remaining alias images.

3.2 Comparison to direct summation

The effects of aliasing are most effectively estimated comparing the density field in Fourier space obtained by a given interpolation scheme with the density field obtained by direct summation to the same grid, where they are absent. Along the lines of the tests presented in Colombi et al. (2009), in this section we consider two different particle distributions both relevant for large-scale structure studies: an *N*-body simulation evolved to redshift zero on a relatively small box (therefore characterized by significant non-linearities) and a distribution obtained in the ZA at high redshift. Due to the significant numerical resources required by the direct summation, we will consider distributions of a relatively low number of particles.

For the *N*-body simulation, we make use of the controlled numerical experiment described in Colombi et al. (2009), run on a box of size $L = 50\,h\,{\rm Mpc}^{-1}$ of side with $N_{\rm P} = 128^3$ particles, and publicly available in the POWMES package as a test for the code.

In this case, before presenting the comparison between power spectra and to underline the fact that the interlacing correction acts at the level of density field, we show a comparison between the amplitudes (as $\ln|\delta(\boldsymbol{k})|$, Fig. 3) and phases ($\phi = \arctan\left[{\rm Im}\,\delta(\boldsymbol{k}) / {\rm Re}\,\delta(\boldsymbol{k})\right]$, Fig. 4) of the density in Fourier space. Since small-scales modes dominate the scatter plot due to their larger number, we show large-scale modes characterized by $|\boldsymbol{k}| \leq 0.7\, k_{\rm Nyq}$ by a darker shade (red or blue in the colour figure), while all others are denoted by a lighter shade (orange or cyan). While this is a rather qualitative comparison, it is evident that both the choice of the assignment scheme and the correction provided by interlacing play an important role in the reducing the scatter, and this is true for the amplitudes and phases alike. In particular, we can notice how the benefits of PCS interpolation and interlacing extend to all modes, all the way up to the Nyquist frequency, while in the other cases small scales are affected by a significant scatter.

Downloaded from http://mnras.oxfordjournals.org/ at SISSA on October 12, 2016

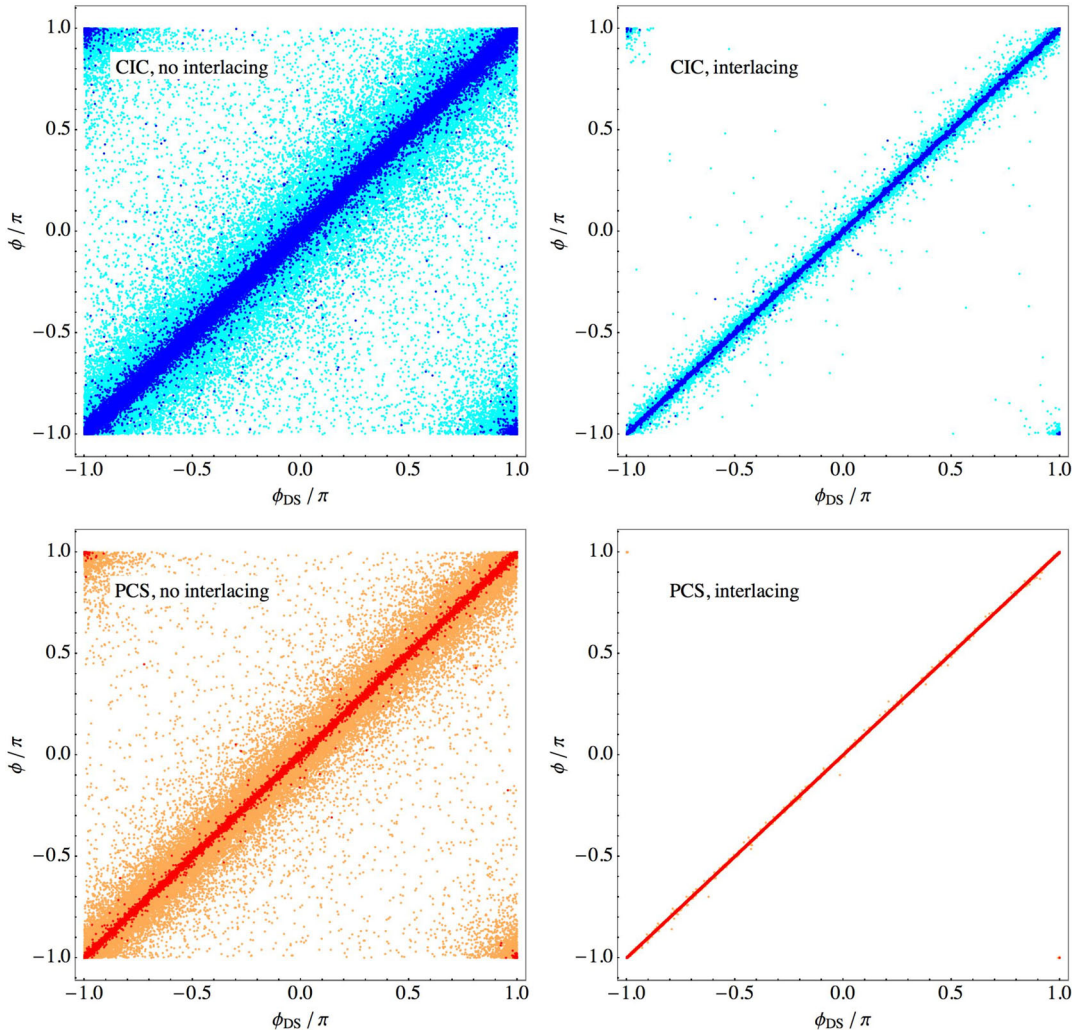

Figure 4. Same as Fig. 3, but comparing the phases of the Fourier-space mode, $\phi = \arctan[\mathrm{Im}\,\delta(\boldsymbol{k}) / \mathrm{Re}\,\delta(\boldsymbol{k})]$.

More quantitative results can be obtained by looking at measurements of the power spectra. Fig. 5 shows the comparison between the simulation power spectrum obtained by different mass assignment schemes and the one obtained by direct summation. In particular, the left-hand panel shows the absolute value of the relative difference between the cross-power spectrum obtained from the grid-based (and window-corrected) density field $\delta^G(\boldsymbol{k})$, with the one obtained by direct summation, $\delta(\boldsymbol{k})$, that is $P_{\mathrm{G-DS}} \sim \langle \delta^G(\boldsymbol{k})\, \delta(-\boldsymbol{k}) \rangle$, to the autopower spectrum $P_{\mathrm{DS}} \sim \langle |\delta(\boldsymbol{k})|^2 \rangle$, in short

$$\left| \frac{P_{\mathrm{G-DS}}(k)}{P_{\mathrm{DS}}(k)} - 1 \right|.$$

This quantity provides an estimate of the error induced on the density field itself by the grid assignment and aliasing. The right-hand panel of Fig. 5 shows instead the relative difference between the autopower spectra $P_{\mathrm{G}} \sim \langle |\delta^G(\boldsymbol{k})|^2 \rangle$ and P_{DS},

$$\left| \frac{P_{\mathrm{G}}(k)}{P_{\mathrm{DS}}(k)} - 1 \right|,$$

larger roughly by a factor of 2, as one can expect. Both auto- and cross-power spectra are corrected for shot-noise simply by subtracting the inverse number density of the box. Upper panels assume an interpolation grid of linear size $N_{\mathrm{G}} = 100$ while lower panels assume $N_{\mathrm{G}} = 256$. In all cases, results are shown as a function of the ratio of the wavenumber k to the Nyquist frequency $k_{\mathrm{Nyq}} \equiv \pi\, N_{\mathrm{G}}/L$, L being the size of the box. In this way, it is easy to read-off the reach in the range of validity of each interpolation scheme in terms of the relative fraction of the Nyquist. For instance, the commonly used CIC scheme, when no aliasing correction is applied, provides a per cent level accuracy only up to 0.6 k_{Nyq}. The immediate consequence of this fact is that if per cent accuracy is required on a given range of scale, to avoid unwanted aliasing contributions the interpolation grid should be ~ 6 ($1/0.6^3$, in three dimensions) times larger than the one naively expected in the case such accuracy could be reached over all wavenumbers, resulting in much larger numerical effort. The situation is even worse if the required accuracy is at the 0.1 per cent level; in this case, the CIC reach is $k \lesssim 0.4\, k_{\mathrm{Nyq}}$. Different, higher order interpolation schemes can marginally improve the range of scales over which a given accuracy is recovered, but they show aliasing components converging to the same value (at tens of per cent level) as the Nyquist frequency is approached.

Such behaviour is significantly reduced, instead, when the interlacing technique is applied. In this case, a 0.1 per cent accuracy is reached, with a CIC scheme, all the way up to the Nyquist, while PCS provides 0.01 per cent accuracy at the Nyquist frequency and reaches the limits imposed by single precision arithmetic ($\sim 10^{-7}$) used in this test at low wavenumbers.

Downloaded from http://mnras.oxfordjournals.org/ at SISSA on October 12, 2016

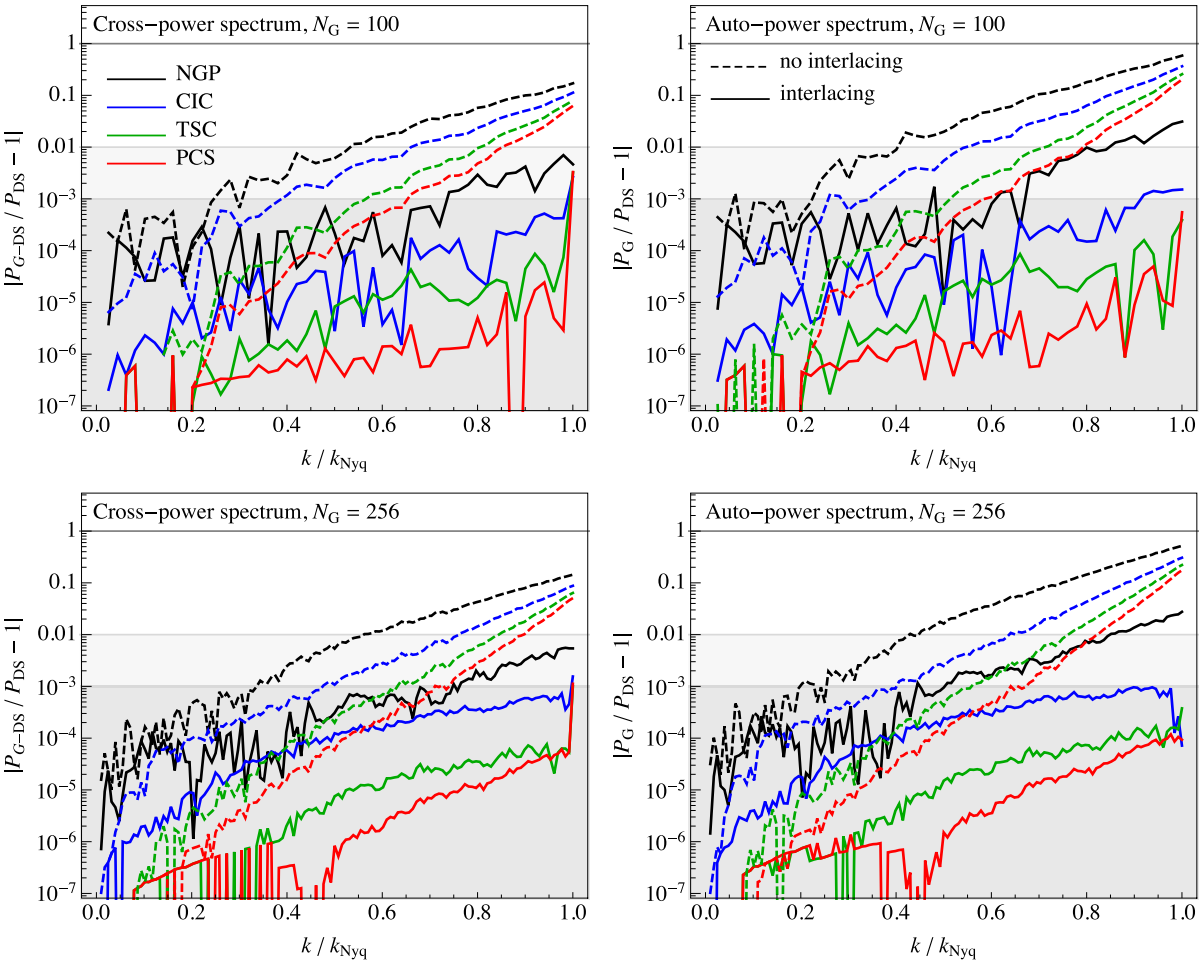

Figure 5. Comparison between the power spectrum measured by FFT of a grid interpolated field and the same quantity obtained by direct summation as a function of the wavenumber in units of the Nyquist frequency. The left-hand panel show the absolute value of the relative difference between the cross-power spectrum of the grid-based, window-corrected field with the direct summation density field, $P_{G-DS} \sim \langle \delta^G(\boldsymbol{k})\, \delta(-\boldsymbol{k}) \rangle$ to the autopower spectrum $P_{DS} \sim \langle |\delta(\boldsymbol{k})|^2 \rangle$. The right-hand panel shows instead the relative difference between the autopower spectra $P_G \sim \langle |\delta^G(\boldsymbol{k})|^2 \rangle$ and P_{DS}. Results in the top panels assume a (linear) FFT grid of $N_G = 100$ while the bottom panels assume $N_G = 256$. All measurements are performed on the N-body simulation described in Colombi et al. (2009).

It should be noted, however, that these results so far are specific to an N-body simulation at $z = 0$ run on a relatively small box. Since aliasing depends on the small-scale power, it is important to consider different distributions to have a more complete picture of the problem. As an additional, alternative test, we consider a distribution of 360^3 particles obtained in the ZA at redshift $z = 50$ in a box of side $L = 2400\,h\,\mathrm{Mpc}^{-1}$. Fig. 6 shows the same quantities as Fig. 5, but, in this case, we limit the comparison to a grid of linear size $N_G = 128$. At the large redshift assumed, with the particle distribution corresponding to the typical initial conditions of an N-body simulation, the displacements from the initial grid are very small respect to the grid scale and no shot-noise correction is applied. We see from this figure that NGP cannot capture the small displacements (which is not surprising) while CIC also has significant systematic errors even when interlacing (which does not help as much as in the previous distribution). It is therefore remarkable that, even for such a peculiar particle distribution, interlacing provides an accuracy better than 0.1 per cent level for TSC and 0.01 per cent for PCS.

3.3 Comparison to analytical predictions

A further test of a power spectrum estimator would be given by a particle distribution with a known power spectrum. Clearly, as the accuracy levels being tested are well below the per cent level, the expected systematic error on such theoretical power spectrum should correspondingly be very small and this is a quite difficult goal to achieve. In principle, however, the ZA provides a particle distribution with a non-linear power spectrum that can be computed exactly. This is given by

$$P_{ZA}(k) = \int \frac{d^3r}{(2\pi)^3}\, e^{i\boldsymbol{k}\cdot\boldsymbol{r}} \left[e^{-k^2\sigma_v^2 - I(\boldsymbol{k},\boldsymbol{r})} - 1 \right], \tag{48}$$

where $I(\boldsymbol{k},\boldsymbol{r}) \equiv \int d^3q\, (\boldsymbol{q}\cdot\boldsymbol{k})^2 \cos(\boldsymbol{q}\cdot\boldsymbol{r})\, P_L(q)/q^4$ and $\sigma_v^2 \equiv I(k,0)/k^2$ (Bond & Couchman 1988; Schneider & Bartelmann 1995; Taylor & Hamilton 1996). In what follows, the ZA theoretical predictions are computed assuming an infrared cutoff given by the fundamental frequency of the box and an ultraviolet cutoff corresponding to the Nyquist frequency of the initial particle grid.

Downloaded from http://mnras.oxfordjournals.org/ at SISSA on October 12, 2016

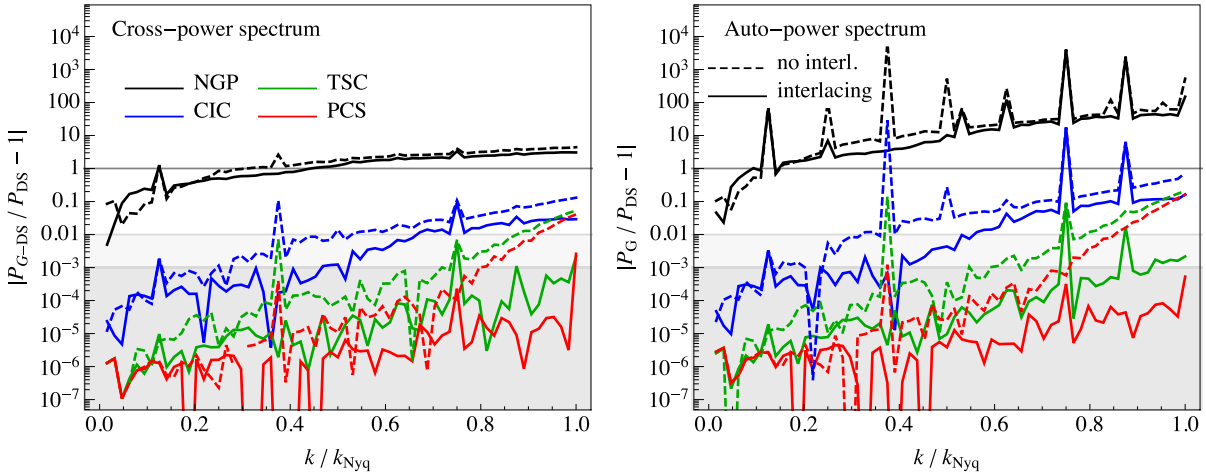

Figure 6. Same as Fig. 5, but for a assuming a distribution of 360^3 particles obtained in the ZA at redshift $z = 50$, therefore similar to the initial conditions of an N-body simulation. All measurements assume a density grid of linear size $N_G = 128$.

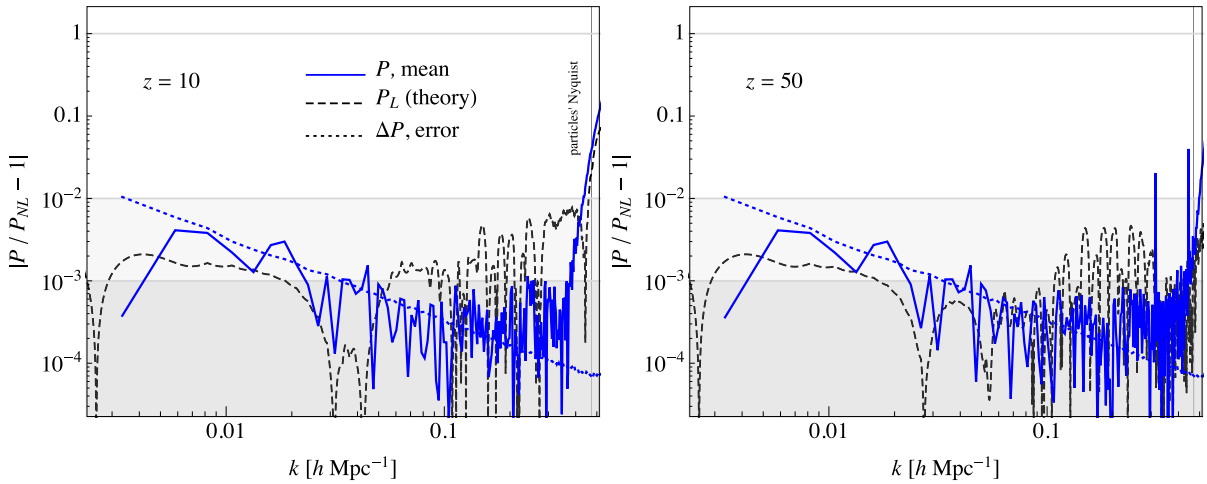

Figure 7. Absolute value of the relative difference between the mean power spectrum measured in 1000 ZA realizations (on a FFT grid of linear size $N_G = 480$, blue curves) and the non-linear prediction of equation (48). Also shown is the error on the mean (blue, dotted curves) and the linear prediction (black, dashed curves). Left-hand panel assumes redshift $z = 10$, right-hand panel $z = 50$. The vertical lines mark the Nyquist frequency of the ZA realizations, beyond which we expect discreteness corrections to be relevant.

We run 1000 realizations of the ZA with 360^3 particles in a box of side $L = 2400\,h^{-1}$ Mpc, at redshifts $z = 10$ and 50. Fig. 7 shows the absolute value of the relative difference between the mean of the measured power spectra (on an FFT grid of linear size $N_G = 480$, *blue curve*) and the non-linear prediction. Also shown is the linear prediction (*black, continuous curve*) and the error on the mean (*blue, dotted curve*). One can notice that our measurements, done with PCS interpolation and interlacing, show the expected agreement with the non-linear prediction while departing from the linear one despite the very small difference (of the order of 0.1 per cent) between the two. Note that we do *not* subtract any shot-noise component in this case: the ZA displacements at high redshift are very small w.r.t. the initial interparticle distance defined by the grid and no significant shell-crossing occurs at small scales. The plots are limited by the particle's Nyquist frequency, that is the Nyquist frequency of the initial ZA grid, which has a smaller value than Nyquist frequency of the FFT grid. In fact, one can notice that some additional component to the measured power spectrum appears near the particle's Nyquist frequency, shown in the plots by a vertical line. This is likely due to the discrete nature of the ZA realizations and therefore arising from the interplay between the FFT grid size and the particle grid (see Gabrielli 2004; Colombi et al. 2009, for a theoretical description of these effects). We did not attempt to derive analytically the expected correction, but we compared the results obtained from realizations characterized by a different number of particles (360^3 and 400^3, not shown) keeping all other variables unchanged. We did notice that the additional component near the Nyquist frequency is different for the two distributions and it is actually reduced for the one with the largest particle density.

3.4 Comparison to POWMES

The POWMES code (Colombi et al. 2009), based on a Fourier–Taylor expansion allows for a determination of the power spectrum with arbitrary accuracy at the expenses of numerical resources. In practice, it reduces the contribution of aliasing by increasing the order

Downloaded from http://mnras.oxfordjournals.org/ at SISSA on October 12, 2016

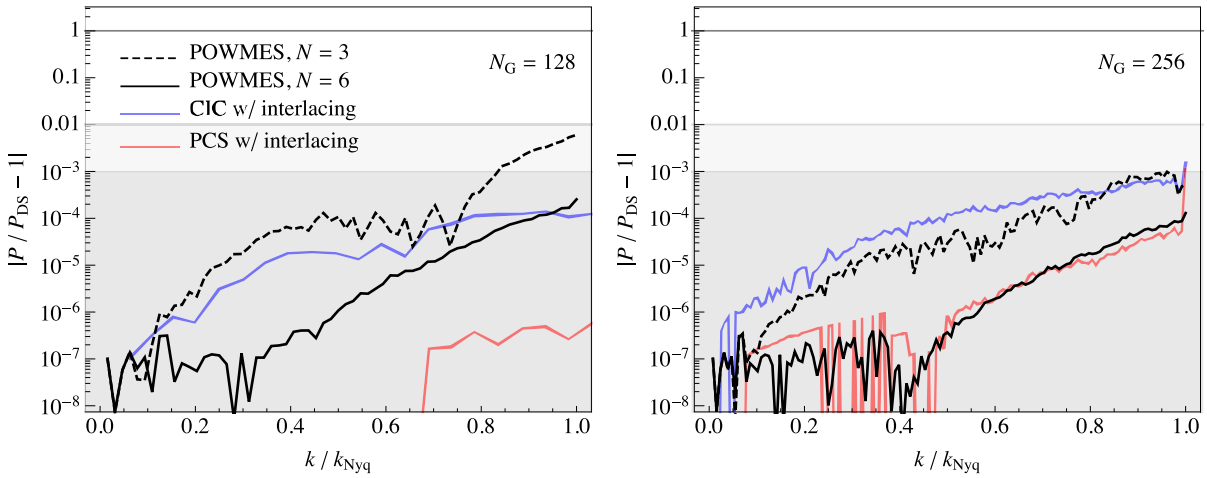

Figure 8. Relative difference between the POWMES (black curves) measurements and our measurements (blue and red curves) with the direct summation result performed over the N-body simulation described in Section 3.2. Dashed and continuous black curves assume, respectively, the order $N = 3$ and 6 in the Taylor expansion of POWMES. Blue and red continuous curves correspond, respectively, to the CIC and PCS interpolation schemes, both with interlacing. The left-hand panel assumes a grid of size $N_G = 128$, while the right-hand panel assumes $N_G = 256$.

N of the expansion, while providing an estimate of the residuals at each order. However, it thus requires a number of FFTs at each order given by $N_{FFT} = (N + 3)!/(N!\,3!)$, so that the total computational cost is $\mathcal{O}(N_{FFT} \times N_G^3 \ln N_G)$, where N_G is the linear size of the grid.

Fig. 8 shows a comparison between measurements of the POWMES code and CIC and PCS interpolation with the interlacing scheme proposed in this paper, in terms of their relative difference with the direct summation measurement of the power spectrum. For the particle distribution, we assume again the test N-body simulation of Colombi et al. (2009).

Within the POWMES results themselves, one can notice a clear improvement when comparing different orders in the Fourier–Taylor expansion (for a given grid size). This comes, however at a large computational cost. In this example, the expansion orders $N = 3$ and 6 for POWMES correspond to a number of FFTs of $N_{FFT} = 20$ and 84. Remarkably, a comparable improvement (or better, depending on N_G) can be achieved moving from CIC to PCS interpolation while performing interlacing. In this case, we only require two FFTs.

4 HIGHER ORDER CORRELATIONS

A positive aspect of correcting for aliasing at the level of the density field itself consists in extending its benefits to the estimation of all higher order correlation functions, not just to power spectrum measurements. In this section, we consider the case of the bispectrum, i.e. the three-point function in Fourier space.

A general expression for the estimator of the bispectrum function of a triplet of wavenumbers $\boldsymbol{k}_1$, $\boldsymbol{k}_2$ and $\boldsymbol{k}_3$ in the case of a simple geometry is given by

$$\hat{B}(k_1, k_2, k_3) \equiv \frac{1}{V_B} \int_{k_1} \mathrm{d}^3 q_1 \int_{k_2} \mathrm{d}^3 q_2 \int_{k_3} \mathrm{d}^3 q_3\, \delta_D(\boldsymbol{q}_{123}) \times \delta_{\boldsymbol{q}_1}\, \delta_{\boldsymbol{q}_2}\, \delta_{\boldsymbol{q}_3}, \tag{49}$$

where the integrals are assumed to be over a spherical shell of size Δk, with radius centred at $\boldsymbol{q}_i = \boldsymbol{k}_i$, that is

$$\int_k \mathrm{d}^3 q \equiv \int_{k-\Delta/2}^{k+\Delta k/2} \mathrm{d}q\, q^2 \int \mathrm{d}\Omega, \tag{50}$$

and where the normalization factor V_B, given by

$$V_B(k_1, k_2, k_3) \equiv \int_{k_1} \mathrm{d}^3 q_1 \int_{k_2} \mathrm{d}^3 q_2 \int_{k_3} \mathrm{d}^3 q_3\, \delta_D(\boldsymbol{q}_{123}), \tag{51}$$

is proportional to the number of fundamental triplets $\boldsymbol{q}_1$, $\boldsymbol{q}_2$ and $\boldsymbol{q}_3$ that can be found in the triangle bin defined by the wavenumbers k_1, k_2 and k_3, with width Δk. In both the integrals of equation (49) and equation (51), the Dirac delta ensures that the triplet of $\boldsymbol{q}_i$ actually forms a closed triangle.

4.1 A fast bispectrum estimator

The implementation of the expression in equation (49) can take advantage of the integral representation of the Dirac delta, so that (see Scoccimarro 2015, for extensions to redshift-space)

$$\begin{aligned}\hat{B}(k_1, k_2, k_3) &= \frac{1}{V_B} \int \frac{\mathrm{d}^3 x}{(2\pi)^3} \int_{k_1} \mathrm{d}^3 q_1 \int_{k_2} \mathrm{d}^3 q_2 \int_{k_3} \mathrm{d}^3 q_3 \\ &\quad \times \delta_{\boldsymbol{q}_1}\, \delta_{\boldsymbol{q}_2}\, \delta_{\boldsymbol{q}_3}\, \mathrm{e}^{i\, \boldsymbol{q}_{123} \cdot \boldsymbol{x}} \\ &= \frac{1}{V_B} \int \frac{\mathrm{d}^3 x}{(2\pi)^3} \prod_{i=1}^{3} I_{k_i}(\boldsymbol{x}),\end{aligned} \tag{52}$$

where the integrals

$$I_k(\boldsymbol{x}) \equiv \int_k \mathrm{d}^3 q\, \delta_{\boldsymbol{q}}\, \mathrm{e}^{i\, \boldsymbol{q} \cdot \boldsymbol{x}}, \tag{53}$$

whose number is equal to the number N_k of k-bins we are interested in, can be evaluated as FFTs (scaling as $N_G^3 \ln N_G^3$) and stored in memory. The final integral in equation (52) corresponds to an $\mathcal{O}(N_G^3)$ process. The normalization factor $V_B(k_1, k_2, k_3)$ can also be evaluated in a similar way.

Notice that because of the exponential $\mathrm{e}^{i \boldsymbol{q}_{123} \cdot \boldsymbol{x}}$ in equation (52), this estimator cannot be applied to all values of k_i up to the Nyquist frequency of the box. In fact, for a translation of the wavenumbers $\boldsymbol{q}$ given (in one dimension) by $q_i \to q_i + \frac{2\pi}{L} \frac{N_G}{3}$ where N_G is the grid size and L the linear size of the box, we have $q_{123} \to q_{123} + \frac{2\pi N_G}{L}$ and with $x = m L/N_G$ the exponential factor would be invariant. It follows that the largest value for the wavenumbers k turns out to be $k_{max} = k_f N_G/3$, k_f being the fundamental frequency rather than

Downloaded from http://mnras.oxfordjournals.org/ at SISSA on October 12, 2016

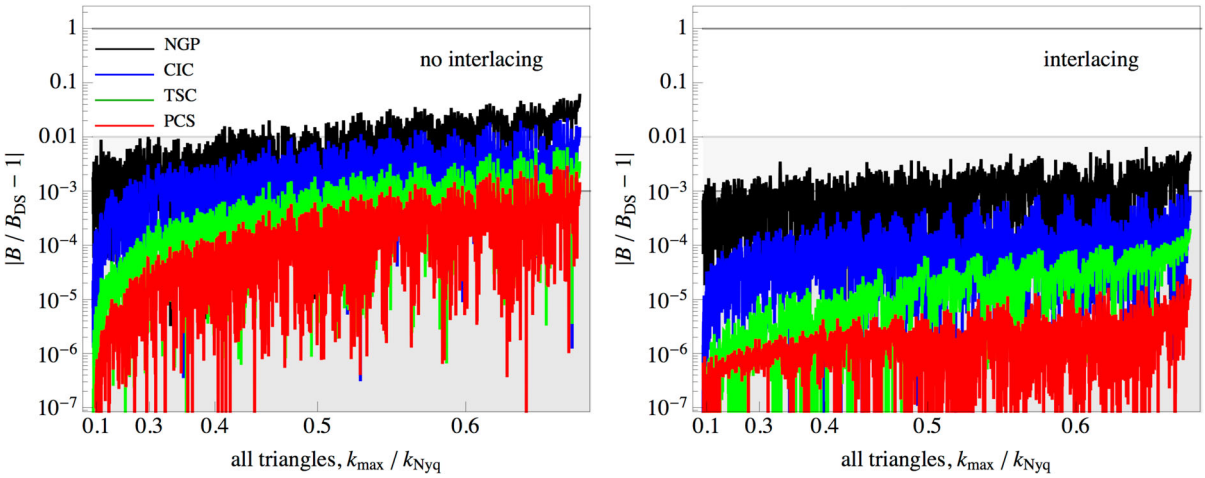

Figure 9. Aliasing effects on the bispectrum. Both panels show the relative difference between the bispectrum measured with distinct interpolation schemes (NGP, CIC, TSC, and PCS, as black, blue, green and red curves, or different shades top to bottom) with respect to the bispectrum measured from the density field estimated by direct summation. Results on the left-hand panel do not implement interlacing, while the results on the right-hand panel do. We show all triangular configurations with triplets (k_1, k_2, k_3) measured in units of the fundamental frequency, k_f, up to $2k_{Nyq}/3$ (see the text for explanation). On the x-axis are shown the values of $k_{max} \equiv \max(k_1, k_2, k_3)$ in units of the Nyquist frequency.

$k_{max} = k_f N_G/2$, the Nyquist, as it is the case for the power spectrum estimator.

This implementation of this estimator has been considered already in the past in the context of the large-scale structure (Scoccimarro 2000; Feldman et al. 2001; Scoccimarro et al. 2001). Note that the expression in equation (52) is analogous to the estimator of the microwave anisotropy bispectrum considered by Komatsu et al. (2002).

4.2 Aliasing contributions on the bispectrum

Despite the efficient bispectrum estimator described above, it is still crucial to limit as much as possible numerical requirements starting with the size of the FFT grid. This is true, in particular, regarding the memory requirement since the implementation of equation (52) benefits from storing in memory the integrals of equation (53), i.e. a number of arrays of size N_G^3 equal to the number of k-bins requested. The interlacing scheme described in the previous section therefore results is particularly useful since it allows us to efficiently use the N_G^3 FFT grid, with the aliasing contribution under control all the way up to the Nyquist frequency.

Fig. 9 shows the relative difference between the measurements of the matter bispectrum obtained from the density interpolated on a grid to the measurements of the same quantity obtained from the density evaluated by direct summation. We assume here the 128^3 particle N-body simulation already considered for the power spectrum tests. All measured triangular configurations are shown, ordered by increasing values of $k_1 \geq k_2 \geq k_3$, k_1 therefore representing the largest value of the triplet. For the reason discussed above, the largest value accessible by the estimator is $k = 2k_{Nyq}/3$. The left-hand panel compares different interpolation schemes without aliasing corrections, while the right-hand panel shows the same results including interlacing. In the latter case, already for the CIC scheme, the aliasing contribution is kept below the 0.1 per cent level, while 0.001 per cent is achieved with PCS interpolation. If no aliasing correction is implemented the error can reach the few per cent level already at $k \sim 0.5\, k_{Nyq}$.

Not surprisingly, these results are largely consistent with those obtained for the power spectrum.

5 CONCLUSIONS

Standard FFT-based, power spectrum estimators routinely employed in the analysis of redshift surveys data sets as well as N-body simulations, suffer from spurious contributions due to aliasing. This well-known problem is often circumvented by limiting the range of scales (wavenumbers) over which the desired accuracy could be achieved. The drawback, clearly, is the inefficient use of numerical resources as this approach clearly requires larger FFT grids than naively expected. This becomes even more problematic for higher order correlations.

Aliasing takes the form of a sum over images, each of them corresponding to the Fourier content displaced by increasing multiples of the sampling frequency of the grid. The strength of the aliasing contributions depends on both the interpolation kernel that goes from objects to density perturbations on the grid and the small-scale modes not supported by the grid. We quantified the systematic error on the power spectrum estimation due to aliasing in two particle distributions relevant for large-scale structure studies: an N-body simulation describing the (non-linear) matter field at $z = 0$ and the distribution obtained by particles displaced from a regular grid according to the ZA at $z = 10, 50$.

By comparing our results to the (aliasing-free) estimation by direct summation, we showed that in the N-body example the resulting error on the power spectrum estimation can be larger than 1 per cent already at scales roughly above half the Nyquist frequency of the grid when using the standard CIC interpolation. If the required accuracy is below the 0.1 per cent level, a reasonable requirement for cosmological applications aimed at the detection of small effects possibly due to non-standard physics, the usable range of scales becomes as restrictive as $k \lesssim 0.4 k_{Nyq}$. The problem is even more severe when a distribution like the one obtained by ZA at large redshift is considered: in this case an accuracy of 1 per cent (0.1 per cent) is only achieved for wavenumbers $k \lesssim 0.3\,(0.2)\, k_{Nyq}$.

Downloaded from http://mnras.oxfordjournals.org/ at SISSA on October 12, 2016

We then revisited a method to reduce the aliasing contribution based on an interlacing technique (see e.g. Hockney & Eastwood 1981; Couchman 1991). We showed that using two interlaced grids removes odd images, which include the dominant contribution to aliasing. We demonstrated that this technique is able to reduce the aliasing contribution below the 0.1 per cent level for practically all wavenumbers, all the way to the Nyquist frequency of the grid, when combined with interpolations schemes of order higher than the CIC. This is true for both the examples mentioned above as well as for a comparison of the mean power spectrum measured from 1000 ZA realizations with the exact theoretical prediction. For the interpolation schemes, we considered the third-order TSC scheme and the fourth-order PCS, which are increasingly smooth schemes constructed by convolving a top-hat function with itself an increasing number of times.

While higher order schemes have the disadvantage of an increased time required to perform the particle assignment (without affecting the necessary memory), the payout in terms of systematic errors in Fourier coefficients can be substantial. At a fixed required systematic error, the algorithm proposed here can actually be more efficient than the standard CIC method. To make systematics in the power spectrum negligible, e.g. 0.01 per cent, one requires from CIC a grid size five times larger in each dimension than PCS with interlacing, which results in eight times more computational cost (and 62 times more memory). Similarly due to the increase in grid size, the FFT step is correspondingly slower in the CIC case.

We remark that the aliasing correction implemented via interlacing is performed on the density field itself and have shown that combining PCS with interlacing gives very accurate Fourier amplitudes and phases of density perturbations compared to the standard CIC method. It therefore improves the estimation of the power spectrum *as well as* any higher order correlation functions evaluated from such density. We showed that this is indeed the case for the bispectrum, by performing comparison to the direct summation results, as done for the power spectrum. Other approaches to limit aliasing effects in the estimation of the power spectrum as the one proposed by Jing (2005) cannot be easily extended to higher order correlation functions.

We believe that the method presented here represent a numerically efficient way to reduce aliasing effects in the measurement of correlation functions of particle distributions in Fourier space, relevant in a variety of cosmological investigations. A code implementing the algorithms here described will be soon made public.

ACKNOWLEDGEMENTS

We thank the referee, Stéphane Colombi, for making the POWMES code public and for useful comments and suggestions that improved the presentation. ES thanks Julien Bel for many discussions and the NYU Dept. of Physics and the Institut des Ciències de l'Espai for hospitality during the completion of this project. MC has been partially funded by AYA2013-44327 and acknowledges support from the Ramon y Cajal MICINN programme. RS was partially supported by NSF grant AST-1109432, and HMPC was supported by NSERC.

REFERENCES

Bond J. R., Couchman H. M. P., 1988, in Thorne K. S., ed., Proceedings of the 2nd Canadian Conference on General Relativity and Relativistic Astrophysics, $w_{gg}(\theta)$ as a Probe of Large-Scale Structure. World Scientific Publishing Company, p. 385
Chaniotis A. K., Poulikakos D., 2004, J. Comput. Phys., 197, 253
Colombi S., Jaffe A., Novikov D., Pichon C., 2009, MNRAS, 393, 511
Couchman H. M. P., 1991, ApJ, 368, L23
Couchman H. M. P., 1999, in Miyama S. M., Tomisaka K., Hanawa T., eds, Astrophysics and Space Science Library, Vol. 240, Numerical Astrophysics. Kluwer, Dordrecht, p. 1
Cui W., Liu L., Yang X., Wang Y., Feng L., Springel V., 2008, ApJ, 687, 738
Feldman H. A., Frieman J. A., Fry J. N., Scoccimarro R., 2001, Phys. Rev. Lett., 86, 1434
Gabrielli A., 2004, Phys. Rev. E, 70, 066131
Haugbølle T., Frederiksen J. T., Nordlund A., 2013, Phys. Plasmas, 20, 062904
Hockney R. W., Eastwood J. W., 1981, Computer Simulation Using Particles. McGraw-Hill, New York
Jasche J., Kitaura F. S., Ensslin T. A., 2009, preprint (arXiv:0901.3043)
Jing Y. P., 2005, ApJ, 620, 559
Komatsu E., Wandelt B. D., Spergel D. N., Banday A. J., Gorski K. M., 2002, ApJ, 566, 19
Laureijs R. et al., 2011, preprint (arXiv:1110.3193)
Levi M. et al., 2013, preprint (arXiv:1308.0847)
Peebles P. J. E., 1980, The Large-Scale Structure of the Universe. Princeton Univ. Press, Princeton, NJ
Schneider P., Bartelmann M., 1995, MNRAS, 273, 475
Scoccimarro R., 2000, ApJ, 544, 597
Scoccimarro R., 2015, Phys. Rev. D, 92, 083532
Scoccimarro R., Feldman H. A., Fry J. N., Frieman J. A., 2001, ApJ, 546, 652
Taylor A. N., Hamilton A. J. S., 1996, MNRAS, 282, 767
Yang Y.-B., Feng L.-L., Pan J., Yang X.-H., 2009, Res. Astron. Astrophys., 9, 227

This paper has been typeset from a TEX/LATEX file prepared by the author.

Downloaded from http://mnras.oxfordjournals.org/ at SISSA on October 12, 2016